On the non-linear effects in graphene devices

2014 J. Phys. D: Appl. Phys. 47 094007

(http://iopscience.iop.org/0022-3727/47/9/094007)

IOP Publishing Journal of Physics D: Applied Physics
J. Phys. D: Appl. Phys. **47** (2014) 094007 (10pp) doi:10.1088/0022-3727/47/9/094007

On the non-linear effects in graphene devices

Viet Hung Nguyen[1,2,4], Alfonso Alarcón[1], Salim Berrada[1], Van Nam Do[3], Jérôme Saint-Martin[1], Damien Querlioz[1], Arnaud Bournel[1] and Philippe Dollfus[1]

[1] Institute of Fundamental Electronics (IEF), Univ. Paris-Sud, CNRS, UMR 8622, Orsay, France
[2] Institute of Physics, Center for Computational Physics, Vietnamese Academy of Science and Technology, Hanoi, Vietnam
[3] Advanced Institute for Science and Technology (AIST), Vietnam and International Center for Computation Materials Science (ICCMS), Hanoi University of Science and Technology (HUST), Hanoi, Vietnam

E-mail: philippe.dollfus@u-psud.fr

Received 15 April 2013, revised 25 June 2013
Accepted for publication 27 June 2013
Published 12 February 2014

Abstract

We study several graphene devices able to generate non-linear effects in the current–voltage characteristics and in particular negative differential resistance (NDR) effects. This theoretical investigation is based on numerical charge transport simulation in the Green's function approach applied to a tight-binding Hamiltonian for particles in graphene. Depending on the device, the physical mechanism involved in the NDR effect may be different: (i) the mismatch of modes between left and right sides of a P^+/P zigzag ribbon junction, (ii) the modulation of interband tunnelling in P/N junctions (tunnel diodes and tunnel field-effect transistors) or (iii) the modulation of chiral tunnelling in 'conventional' graphene transistors. We emphasize the advantages of exploiting different approaches of bandgap engineering in the form of graphene nanoribbons (GNRs) or nanomesh lattices (GNM), the latter resulting from a periodic array of nanoholes in graphene sheets. In particular, such nanostructuring allows us to design position-dependent bandgaps in devices, which is shown to make possible the optimization of device operation and, here, to get very high peak-to-valley ratio of the NDR. In the case of GNR nanostructuring, it is shown that appropriate bandgap engineering can even make the current–voltage characteristics of tunnel diodes weakly sensitive to the atomic edge disorder. Finally, GNM lattices are shown to be a very promising way to open large bandgaps in wide sheets of graphene and to introduce bandgaps locally with a view to optimizing the device operation and performance.

(Some figures may appear in colour only in the online journal)

1. Introduction

The exceptional intrinsic electronic properties of graphene as high carrier mobility [1, 2] and high critical current density [3] make this material an excellent candidate for high-frequency applications [4, 5]. Beyond the usual linear or saturation behaviours expected to occur in transistors, non-linear effects such as the negative differential resistance (NDR) in the current–voltage characteristics may be of strong interest in designing devices for high-speed analogue applications and memories [6]. Hence, strong efforts have been devoted recently to investigating the possibility to generate a negative differential conductance or transconductance in graphene devices, based on various physical mechanisms.

Using wide graphene sheets, a possible NDR effect has been shown to occur in single-barrier graphene structures, though the occurrence of band-to-band (BTB) tunnelling in gapless graphene should be an obstacle to this effect [7, 8]. A stronger NDR has been predicted to occur in Esaki-like PN junctions (tunnel diodes), the operation of which is controlled

[4] Present address: L_Sim, SP2M, UMR-E CEA/UJF-Grenoble 1, INAC, Grenoble, France.

by the interband tunnelling between the conduction band of the N-doped side and the valence band in the P-doped side. Though small in gapless monolayer and bilayer graphene (BG) sheets [9, 10], this effect may increase significantly if a bandgap can be generated in graphene. A negative transconductance can be obtained in short single-gate gapless BG structures as a consequence of resonant chiral tunnelling [11] while the finite bandgap opened in a double-gate BG structure has been used too to generate an NDR effect [12]. A similar effect has been predicted in double-barrier resonant tunnelling diodes [13, 14], in graphene/BN heterodiodes [15] and in graphene nanoribbon (GNR) superlattices with different ballistic transport regimes, including the resonant tunnelling through the minibands and the Wannier–Stark ladder regime [16]. Additionally, if a magnetic coupling can be induced in the gated part of a graphene sheet, as e.g. by proximity effect [17], efficient spin filtering and strong oscillation/switching of spin polarization can be achieved [8], especially in BG structures [18].

The nanostructuring of graphene into GNRs offers additional possibilities likely to enhance the non-linear effects in I–V characteristics. The effect of parity selective rule [19] existing in perfect zigzag (Z) GNRs with an even number of zigzag lines defining the ribbon width has been predicted to generate an NDR [20]. Regardless of the width of the GNR, the mismatch of modes between the left and right sides of a ZGNR junction may also induce an NDR [21, 22]. An NDR has been also observed in different kinds of armchair GNRs working in resonant tunnelling regime [23, 24] and in GNRs made of armchair and zigzag sections of different widths [25–27].

Finally, it should be noted that an NDR behaviour has been observed experimentally in long-channel graphene field-effect transistors (GFETs) [28, 29] for particular values of gate voltage. It has been explained either as a consequence of the distribution of high local resistance between the N-doped and the P-doped regions of the channel [28] or as resulting from a complex interplay among self-heating, hot carrier injection to gate oxide and minority carrier injection from drain [29].

The objective of the present article is to review and synthesize different devices and related physical phenomena likely to provide non-linear effects in the I–V characteristics and especially NDR effects. The analysis will be made on the basis of numerical simulations of quantum transport. It will include P^+/P zigzag GNR junctions with the effect of mismatch of modes, GNR and graphene nanomesh (GNM) tunnel diodes with the effect of interband tunnelling, tunnel field-effect transistors (FETs) where the interband tunnelling can be modulated, and 'conventional' GFET with the effect of chiral tunnelling. In particular, it will be shown that the bandgap engineering in GNRs and in GNMs made of lattices of nanoholes may not only enhance the peak-to-valley ratio of tunnel diodes but can also make the I–V characteristics weakly sensitive to the doping profile and to the atomic disorder that is the usual drawback of GNR devices. Additionally, the tunnel field-effect transistor (TFET), which is the transistor counterpart of the tunnel diode, will be shown to make the NDR effect strong and tunable by the gate voltage. Finally, the analysis of ballistic short-channel GFETs will show that the modulation of chiral tunnelling at negative gate voltage may also lead to an NDR effect, especially if a bandgap is opened in the graphene sheet.

The bandgap opening is actually a crucial point to achieving strong non-linear effects. The most common approach consists in cutting 2D graphene sheets into 1D narrow ribbons, i.e. in GNRs. However, for the bandgap to be significant, the GNR width should be smaller than about 3 nm, which is difficult to achieve, gives rise to problems of reproducibility and edge roughness control, and provides limited driving current. Opening bandgap in 2D graphene sheets is theoretically possible in the case of Bernal stacking of graphene on hexagonal BN sheet. Bandgaps of 53 and 100 meV have been predicted theoretically [30, 31] and may even increase up to more than 200 meV under external pressure [32, 33]. Additionally, when graphene is reported on h-BN, the interface is clean enough to make the mobility almost as high as in suspended graphene [2], which should allow reaching ballistic transport at room temperature. In the case of Bernal-stacking bilayer graphene, the vertical electric field that can be induced in a double-gate structure may generate a controllable bandgap of up to 250 meV [34, 35]. Alternatively, the opening of a bandgap in large sheets of graphene has been demonstrated by punching a high-density array of periodic nanoholes [36, 37]. Depending on the neck width, the meshing orientation and the shape of holes, bandgaps higher than 0.5 eV could be achieved [38, 39], which opens new routes of band structure engineering for graphene applications, including waveguides [40] and magnetic structures [41]. These different possibilities of bandgap opening in monolayer graphene have been exploited in the present work.

2. Model

In our model the Hamiltonian of the graphene lattice is considered via a nearest-neighbour tight-binding approximation [42], i.e.

$$H_{\mathrm{tb}} = \sum_n \varepsilon_n \left|\right\rangle \left\langle n\right| - t \sum_{\langle n,m\rangle} \left[\left|\right\rangle \left\langle m\right| + \left|\right\rangle \left\langle n\right|\right], \qquad (1)$$

where n and m refer to the atomic sites of the 2D lattice, ε_n is the on-site energy and $t = 2.7\,\mathrm{eV}$ is the next-neighbour hopping energy [43]. In the case of GNRs with armchair edges (AGNRs) the bond relaxation at the edges is taken into account by using a different hopping energy $t_{\mathrm{e}} = 3.02\,\mathrm{eV}$ for the edge bonds instead of $t = 2.7\,\mathrm{eV}$ for the other bonds [44]. In gapless pristine graphene the two carbon atoms of the elementary cell belong to the triangular sublattices A and B, respectively [45] and have the same on-site energy. If the difference of on-site energy $\Delta = \varepsilon_{\mathrm{A}} - \varepsilon_{\mathrm{B}}$ between A and B atoms is finite, the inversion symmetry is broken and a bandgap $E_{\mathrm{G}} = 2\,\Delta$ is opened, as in the case of graphene on h-BN in a Bernal-stacking arrangement. In this case, the energy dispersion close to the Dirac points is well approximated by

$$E\,(\boldsymbol{k}) = \pm\sqrt{\hbar^2 v_{\mathrm{F}}^2 \left(k_x^2 + k_y^2\right) + \Delta^2}, \qquad (2)$$

where $v_{\mathrm{F}} = 3\,a_{\mathrm{c}}\,t/2\,\hbar \approx 10^6\,\mathrm{m\ s^{-1}}$ is the Fermi velocity, $a_{\mathrm{c}} = 0.142\,\mathrm{nm}$ is the carbon–carbon distance and $\boldsymbol{k} = (k_x, k_y)$

is the 2D wave vector. When $\Delta = 0$, the well-known linear form of the graphene band structure is recovered, with conduction and valence band that meet at the K and K′ (Dirac) points of the Brillouin zone, which results in the charge-conjugation symmetry between electron and hole states and the chiral nature of particles [46]. In the case of large graphene sheets, with either uniform of nanomesh lattice, where we can assume the lateral width of the device to be much larger than the channel length, the y direction can be considered through Bloch periodic boundary conditions [47]. The lattice is then split into unit cells and by Fourier transform of the operators in (1) along the Oy direction, the Hamiltonian (1) is rewritten in the form of the sum of decoupled 1D Hamiltonians $\tilde{H}_{1D}(k_y)$ for each discretized value of wave vector k_y [39]. For a given k_y the retarded Green's function is computed in the ballistic approximation as:

$$G(E, k_y) = [(E - i\,0^+)I - H_{1D}(k_y) - \Sigma(k_y)]^{-1}, \qquad (3)$$

where the self-energy $\Sigma(k_y) = \Sigma_S(k_y) + \Sigma_D(k_y)$ describes the coupling between the graphene channel and the semi-infinite source and drain contacts. It can be expressed for the lead α as $\Sigma_\alpha(k_y) = \tau_{D,\alpha}\, g_\alpha(k_y)\, \tau_{\alpha,D}$, where τ is the hopping matrix that couples the device to the lead and $g_\alpha(k_y)$ is the surface Green's function of the uncoupled lead. The surface Green's function is calculated using the fast iterative scheme described in [48]. The local density of states (LDOS) resulting from the source(drain) states is then given by $D_{S(D)} = G\Gamma_{S(D)}G^\dagger$, where $\Gamma_{S(D)} = i\,(\Sigma_{S(D)} - \Sigma^\dagger_{S(D)})$ is the injection rate at source(drain) contact. The Green's functions (3) are solved self-consistently with the Poisson equation. The updated values of potential resulting from Poisson's equation are reintroduced as on-site energies ε_n in (1). In the results presented below, the self-consistence was activated only in the case of transistors (TFETs and GFETs). In the case of PN junctions, the self-consistence has been shown not to change significantly the results [49] and frozen field simulations were performed. The current is finally computed from the Landauer equation as

$$I = \frac{e}{\pi h}\int_{-\infty}^{\infty} dE \int_{BZ} dk_y\, T\left(E, k_y\right)[f_S\,(E) - f_D\,(E)], \qquad (4)$$

where $f_{S(D)}(E)$ is the source(drain) Fermi distribution function, $T(E, k_y) = \mathrm{Trace}[\Gamma_S\, G\, \Gamma_D\, G^\dagger]$ is the transmission probability and the integral over k_y is performed in the first Brillouin zone. For GNR devices, the Green's function is determined using the Hamiltonian (1) and the expression (4) for current becomes

$$I = \frac{2\,e}{h}\int_{-\infty}^{\infty} dE\; T\,(E)\,[f_S\,(E) - f_D\,(E)]. \qquad (5)$$

3. Results

3.1. Zigzag GNR P⁺/P junctions—the effect of mismatch of modes

Wang *et al* explored the transport properties of junctions made of zigzag-edge graphene ribbons (ZGRs) [20] and pointed out that an NDR effect can result from the so-called parity selective rule, very similar to that observed in doped carbon nanotube junctions [50]. Actually, the parity selection rule only exists in ideal ZGNRs with an even number of zigzag lines defining the ribbon width [19]. Here we show that an NDR effect may be obtained whatever the parity of the number of zigzag lines in P⁺/P ZGNR junctions formed by field-effect doping induced by appropriate gate electrodes.

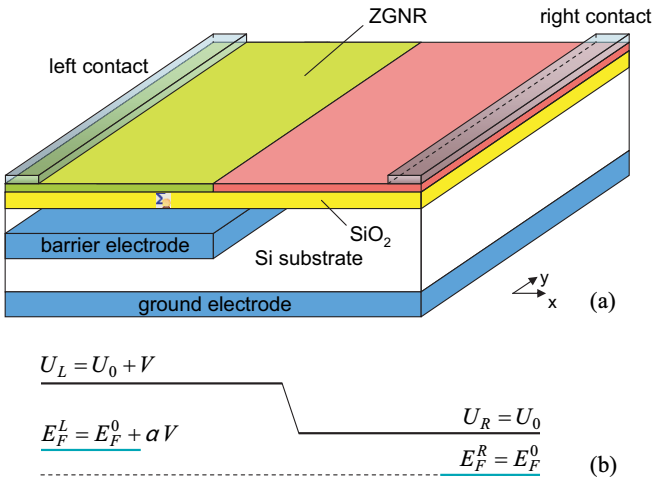

Figure 1. (*a*) Schematic view and (*b*) and profile of the neutrality point along the transport direction of a P⁺/P junction. The P⁺ and P domains are created by field effect by applying different voltages on the barrier and the ground electrodes. The local Fermi levels in the left and right domains are shifted relative to each other by a fraction α (with $\alpha < 1$) of the shift of the neutrality point.

The simulated P⁺/P structure schematized in figure 1(*a*) is basically similar to already fabricated P/N junctions [51]. The GNR is assumed to lie onto the surface of a thin insulating layer. The Si substrate is heavily doped to form the back gate controlling the carrier density in the ribbon by an applied voltage V_{ground}. Another gate buried inside the Si layer is used to form the junction by applying another voltage V. It is named barrier gate and could be a top gate as well. It controls the charge carrier density in the second part of the ribbon to form a P⁺/P junction. Two metallic leads are deposited at the two ends of the ribbon, far enough from the junction. A typical profile of the on-site energy along the transport direction is displayed in figure 1(*b*). In GNR junctions formed by field effect, the Fermi level and the electrostatic potential can be controlled independently by bias and gate voltages. Here, the barrier height of the junction δU can be tuned with respect to the bias applied to the left lead in such a way that if $U_L = U_0 + V$, then $E_F^L = E_F^0 + \alpha V$ with $\alpha \leqslant 1$, which can be achieved by connecting a rheostat between the left lead and the barrier electrode. By adjusting α it is possible to control the position of the conductance gap with respect to the current energy window opened between the Fermi levels of the left and right leads, which can be used to generate an NDR effect, as discussed below.

In figure 2 we plot the I–V characteristics obtained at room temperature for the numbers of zigzag lines $N_{Zline} = 5$ and 6, and for three values of the bias controlling factor $\alpha = 1$, 0.75 and 0.5. For $\alpha = 1$ the NDR effect is observed only for $N_{Zline} = 6$, which is a direct consequence of the parity

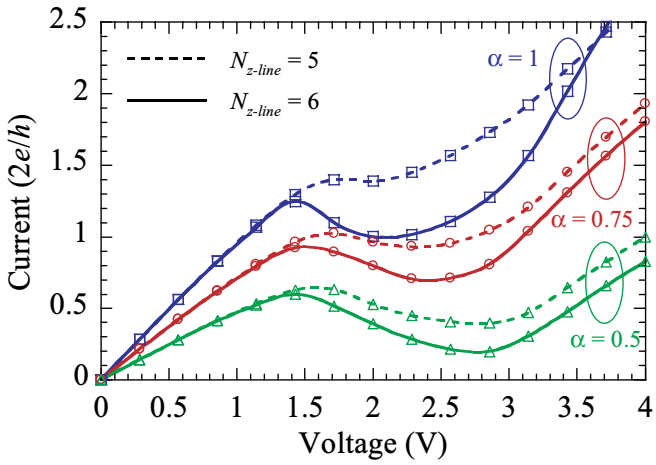

Figure 2. I–V characteristics of the junctions with odd ($N_{\mathrm{Zline}} = 5$, dashed lines) and even ($N_{\mathrm{Zline}} = 6$, solid lines) zigzag line number in the ribbon width for different values of bias controlling factor $\alpha = 1$, $\alpha = 0.75$ and $\alpha = 0.5$. The calculation was made for $E_{\mathrm{F}}^{0} = -1.5$ eV and $T = 300$ K.

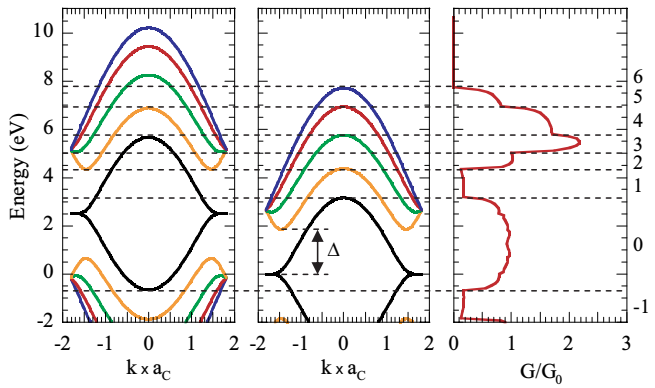

Figure 3. Illustration of the matching of eigen modes in the left and right sides of a P^{+}/P junction in the case where $\delta U > \Delta$. The conductance is plotted in the right panel. Horizontal dashed lines are guides for eyes to define the energy regions numbered on the right side.

selective rule, as previously explained in [19, 20, 52]. Indeed, for even N_{Zline} ribbons, each subband is additionally labelled by a quantum number that reflects the parity of the wave function. The coherent transmission of particles through the junction interface is possible only between modes of the same parity. Consistently, the NDR effect does not occur for the odd value $N_{\mathrm{Zline}} = 5$. However, for $\alpha = 0.75$ and 0.5 the NDR effect is observed whatever the parity of N_{Zline}, though more pronounced in the case $N_{\mathrm{Zline}} = 6$. It is the consequence of another phenomenon that is discussed now.

In ballistic transport regime the conductance G is quantized and its value in a given energy range is proportional to the number of modes available in this range, i.e. $G/G_0 \propto \min\{N_{\mathrm{modes}}^{\mathrm{L}}, N_{\mathrm{modes}}^{\mathrm{R}}\}$, where $G_0 = 2\mathrm{e}^2/h$ and $N_{\mathrm{modes}}^{\mathrm{L/R}}$ are the eigenmode numbers in the left and right sides of the junction, respectively, in the considered energy range. Given Δ the energy separation between the first two subbands, when $\delta U > \Delta$ there is a strong shift between the electronic structures of the left and right sides of the junction, as illustrated in figure 3 for $N_{\mathrm{Zline}} = 5$, which may induce strong variations of

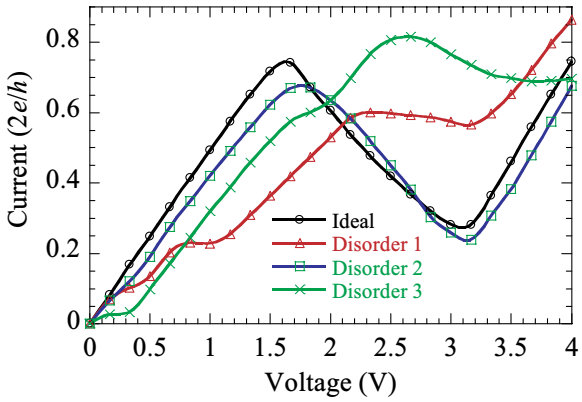

Figure 4. I–V characteristics for different edge-disorder configurations generated randomly from the ideal ribbon with $N_{\mathrm{Zline}} = 6$.

conductance as a function of energy (right panel of figure 3). To understand clearly the behaviour of the conductance plotted in figure 3, we divided the whole energy range into intervals labelled by the integer numbers $-6, -5, \ldots, 0, 1, \ldots, 6$ as indicated in figure 3 by horizontal dashed lines. For instance, in the energy interval (6) we have $N_{\mathrm{modes}}^{\mathrm{L}} = 3$ and $N_{\mathrm{modes}}^{\mathrm{R}} = 0$, and thus $G(6)/G_0 \propto \min\{3, 0\} = 0$. In the other energy intervals, we have, successively, $G(5)/G_0 \propto \min\{3, 1\} = 1$, $G(4)/G_0 \propto \min\{4, 2\} = 2$, $G(3)/G_0 \propto \min\{5, 3\} = 3$, $G(2)/G_0 \propto \min\{2, 3\} = 2$, $G(1)/G_0 \propto \min\{1, 4\} = 1$, and so on. However, it should be noted that due to the strong change of carrier wave vector when crossing the junction, in the intervals (1) and (-1) the conductance G/G_0 is actually much less than the limit value 1, though not equal to 0. This mismatch of modes and their reduced number hence generate a pseudo-gap in the conductance in the energy ranges (1) and (-1). When the factor α is tuned so that this gap enters the energy window $E_{\mathrm{F}}^{\mathrm{L}} - E_{\mathrm{F}}^{\mathrm{R}} = \alpha V$, an NDR effect appears independently of the parity of N_{Zline} (figure 2). The NDR effect is slightly more pronounced for even N_{Zline} because the parity selective rule still plays a role.

However, it is important to consider the influence of unavoidable edge disorder which not only breaks the parity of the zigzag line number but also changes strongly the band structure, tending to make the wave functions localized as in the localized Anderson model [53]. It is known to strongly perturb the transport properties of ZGNRs [54]. Here, the edge roughness is generated using an algorithm that allows randomly removing carbon atoms on the outermost zigzag lines of the ribbon. However, the removing probabilities are not the same for every carbon atom, i.e. an inner atom is removed only if its two neighbour outer atoms are already removed. In figure 4 we plot the I–V characteristics for three disorder configurations and for the perfect ZGNR structure with $N_{\mathrm{Zline}} = 6$ and $\alpha = 0.5$. It is observed that in disordered ZGNR junctions the NDR effect may either fully survive (configuration 2) or almost fully disappear (configurations 1 and 3). However, the NDR may be observed also for perfect ZGNRs of large width (not shown) and in this case the sensitivity to edge effects is expected to be smaller.

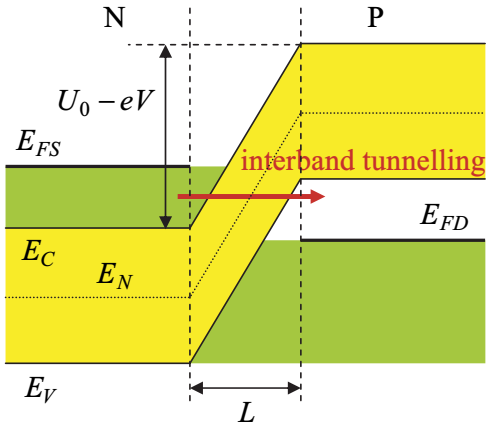

Figure 5. Schematic view of the band structure in a tunnel diode (PN junction) with finite bandgap. The transition region of length L separates the N-doped side from the P-doped side. The interband tunnelling (symbolized by the red arrow) between the conduction band of the N-doped side and the valence band of the P-doped side is the dominant contribution to the current. The quantities E_{FS}, E_{FD}, E_C E_V and E_N stand for the Fermi level in the N side, the Fermi level in the P side, the bottom of conduction band, the top of valence band and the neutrality point, respectively. U_0 is the potential barrier height in the unbiased structure.

3.2. GNR P/N junctions—the effect of interband tunnelling

The NDR effect is known to occur in Esaki P/N junctions (tunnel diodes) based on conventional semiconductors, the operation of which is controlled by the interband tunnelling between the conduction band of the N-doped side and the valence band in the P-doped side, as schematized in figure 5. The junction is characterized mainly by the potential barrier U_0 and the length L of the transition region across which the charge density changes monotonically from N-type to P-type. The peak current is governed by the interband tunnelling through the transition region at low bias while the valley current appears at high bias when the filled states in one side of the junction do not see any free state available for tunnelling in the other side. If the bias voltage is further increased, the thermionic current above the potential barrier leads to the re-increase of current. A similar effect has been predicted to occur also in graphene P/N junction. Though small in gapless monolayer and bilayer graphene sheets [9, 10], this effect may increase significantly if a bandgap can be generated in graphene. It is possible for instance in the case of Bernal stacking of graphene on hexagonal BN sheet [30, 31], or in graphene under external pressure [32, 33] where the bandgap can reach more than 200 meV. Graphene tunnel diodes have been simulated for different values of bandgap and transition length [9]. It has been shown that whatever the bandgap, increasing the transition length does not change the valley current but strongly reduces the peak current. It is due to the large distance to be tunnelled through the bandgap which reduces exponentially the transmission in the interband tunnelling regime. The peak-to-valley ratio (PVR) falls from 123 for $L = 5$ nm to 8.5 for $L = 20$ nm and even 2.5 for $L = 30$ nm (not shown). In spite of promising performance, this high sensitivity to the transition length is obviously an issue for the design of this device.

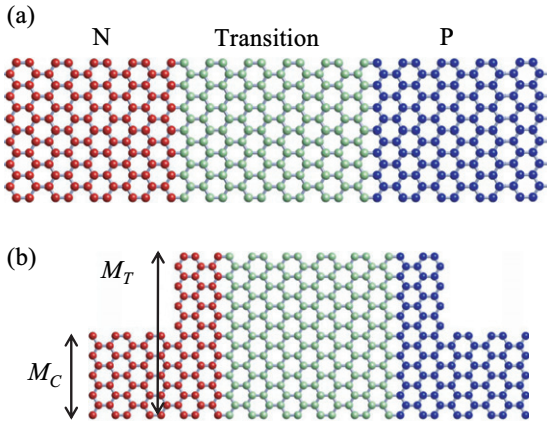

Figure 6. Schematic view of (a) a normal and (b) a T-shape AGNR PN junction. M_C and M_T are the numbers of carbon chains between edges in the contact and the transition regions, respectively.

However, the bandgap nanoengineering of graphene in the form of nanoribbons makes it possible to improve this behaviour. Indeed, cutting a graphene sheet into 1D nanoribbons of a few nanometre widths is the most natural approach to generate a bandgap in graphene. Hence, one can think of designing an AGNR P/N junction as schematized in figure 6(a) to get a high PVR. However, there is no reason for this structure to make the I–V characteristics, and especially the PVR, less sensitive to the length L of the transition region. Regarding this point, we have to keep in mind that if the current peak is controlled by the interband tunnelling, i.e. the bandgap in the transition region, the current valley is mainly controlled by the bandgap in the doped regions which separates the interband tunnelling and the thermionic current. Hence, if we can design a structure where the bandgap is finite in the doped regions and small or even zero in the transition region, we should be able not only to enhance strongly the PVR, but also to make the interband tunnelling weakly sensitive to L. That is why we suggest analyzing the T-shape armchair structure schematized in figure 6(b) where the width is larger in the transition region (with a small bandgap) than in the doped region (with a larger bandgap) [55]. Such GNRs made of alternate sections of different width have been previously suggested to generate a resonant-like behaviour [25], and to enhance the thermoelectric properties of GNRs [26]. The AGNR width is defined here by the number M of carbon chains between the two edges. For instance, in the case $M = 21$, the bandgap reaches 370 meV while it falls to 62 meV for $M = 29$ and re-increases up to 233 meV for $M = 33$.

In figure 7 we plot the I–V characteristics of the normal and T-shape junctions for the transition length $L = 10.2$ nm. As expected, the peak current is strongly enhanced in the T-shape diode and is typically one order of magnitude higher than in the normal junction. Additionally, the valley current in the T-junction appears to be smaller than in the normal ones. It results in behaviour of the PVR very different in these structures, as seen in the inset of figure 7. It is not only much higher in the T-shape junction but it also weakly sensitive to the length L, in contrast to the case of normal junctions of uniform width.

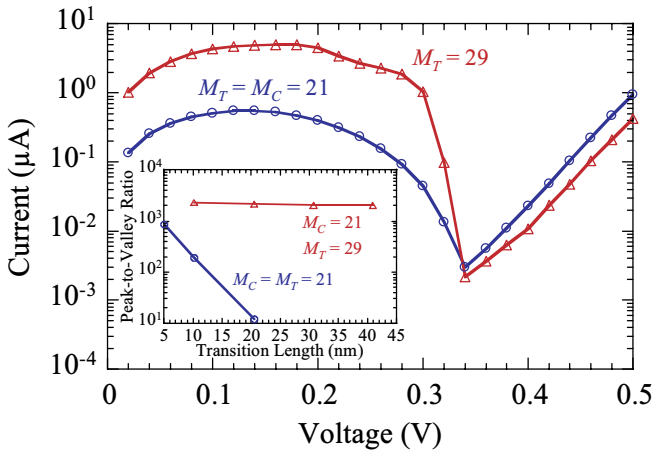

Figure 7. I–V characteristics of a normal P/N junction ($M_C = M_T = 21$) and a T-shape P/N junction ($M_C = 21$, $M_T = 29$) of transition length $L = 10.2$ nm at room temperature. Inset: peak-to-valley ratio in the same types of normal and T-shape junctions as a function of the transition length L. Other parameters: $U_0 = 0.7$ eV.

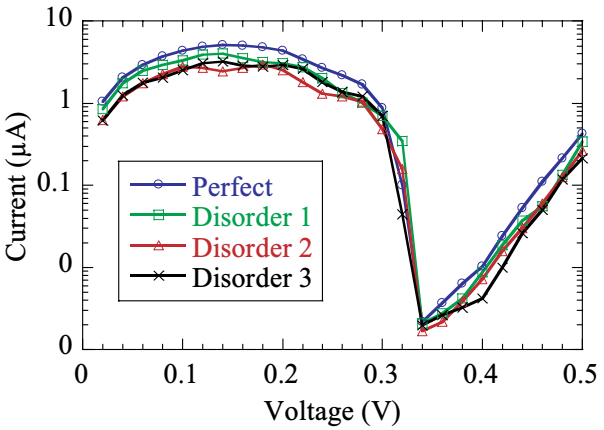

Figure 8. I–V characteristics of T-shape PN junctions ($M_C = 21$, $M_T = 29$) with perfect edges or with different edge-disorder configurations selected randomly.

However, given the strong sensitivity to edge disorder observed above in zigzag P^+/P junctions, it is thus important to evaluate this effect here. In this order, defected T-shape structures have been generated by removing randomly 15% of edge atoms along the structures. Some resulting I–V characteristics are shown in figure 8 and compared to that of the perfect structure. It is remarkable that the valley current is not enhanced but slightly reduced by the disorder and that though the transmission is perturbed the peak current remains high and a large PVR is still achieved. Indeed, the disorder tends to enlarge the bandgap in the doped regions, which is not bad for the device operation. The transition region being small here, it is not strongly perturbed by the random disorder.

Hence, we have shown that it is possible to design AGNR tunnel diodes able to deliver a very high PVR of a few thousand at room temperature. Additionally, using appropriate bandgap engineering, the PVR may be weakly sensitive to the transition length and not strongly degraded by edge disorder. The remaining problem is actually the small current of a few

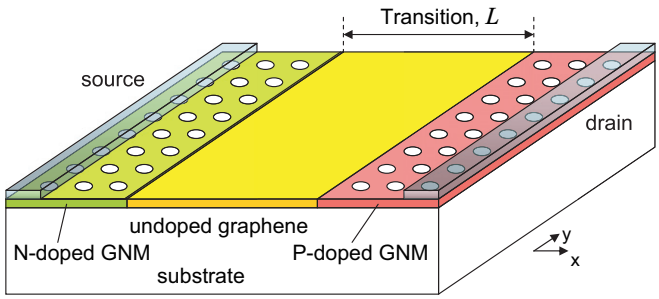

Figure 9. Schematic view of a GNM tunnel diode with the transition region in gapless pristine graphene separating the N- and P-doped parts of the junction.

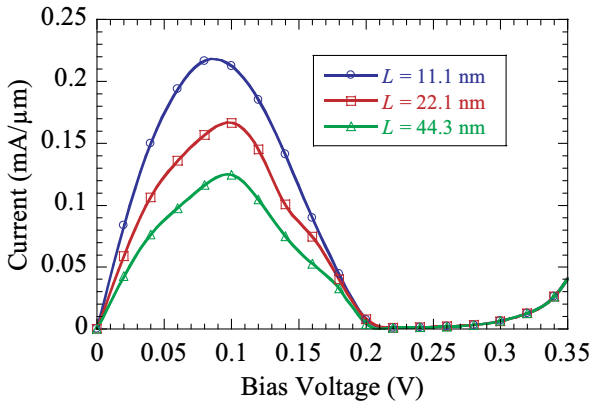

Figure 10. I–V characteristics of GNM tunnel diodes for different values of the length L of the gapless transition region.

micro-amperes that can be driven in such a single narrow ribbon. We will show in the next sub-section that this limitation can be ruled out thanks to the use of GNM lattices which offer similar possibilities of bandgap engineering but on large sheets of graphene.

3.3. GNM P/N junctions

By punching a graphene sheet to form a periodic lattice of nanoholes, the resulting GNM has a bandgap that depends on the neck width, the meshing orientation and the shape of holes. For a given hole shape, due to unavoidable disorder effects, experiments have shown that the bandgap E_G tends to follow a universal dependence on the neck width W_n in the form of $E_G = \alpha/W_n$ [37]. The bandgap may be typically higher than 0.4 eV for a hole distance of about 3 nm [39].

We have considered here a perfect nanomesh lattice with nanoholes corresponding to the removal of 24 carbon atoms, separated by the distances $W_x = 4.8$ nm and $W_y = 2.46$ nm. This configuration leads to the bandgap $E_G = 270$ meV [56]. This GNM has been used to design a P/N junction following the same principle as in the T-shape GNR junction. It is schematized in figure 9. The transition region is made of gapless pristine graphene and is sandwiched by two doped GNM regions. The gapless central region is expected to enhance the interband tunnelling and to make the peak current and the PVR weakly sensitive to the length L of the transition region. It is indeed what is observed in the I–V characteristics

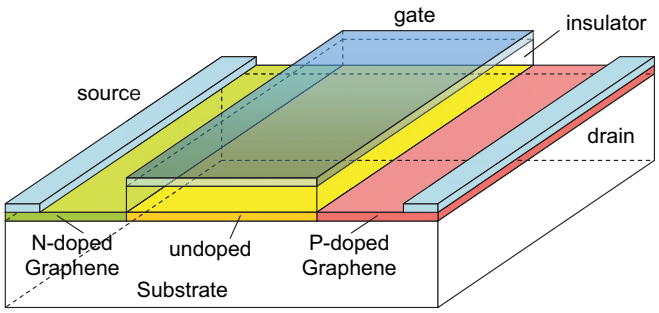

Figure 11. Schematic view of the simulated TFET.

plotted in figure 10. The NDR effect remains strong even for the transition length as high as $L = 44.3$ nm, with a PVR of 105 instead of 197 for $L = 11.1$ nm, which is a remarkable and promising result with a view to achieving NDR devices on large sheets of graphene, with high peak current. One remaining issue that should be considered when designing GNM devices is related to the atomic edge disorder of holes. In principle, this disorder can affect detrimentally the output current. However, in a recent work [39], we demonstrated that the use of suitable GNM sections of finite length in the two doped regions allows us to avoid this effect to a large extent while good device performance is still obtained. Hence, this device is likely to offer reduced problems of reproducibility and variability which are usually considered as a strong issue for the integration of nanodevices, especially when their operation is based on a tunnelling current.

3.4. TFET—the control of interband tunnelling

The TFET is the transistor counterpart of the tunnel diode. In this device, the interband (or band-to-band) tunnelling between the P-doped side and the N-doped side can be tuned by the gate voltage applied on the central region of the device [49]. It is currently considered as a promising device for low-power digital applications thanks to the steep subthreshold slope it is expected to provide, i.e. less than the usual limit of 60 mV/decade at room temperature [57]. Additionally, it may exhibit an NDR in the I–V characteristics [58] as in the tunnel diode. Hence, the TFET offers the possibility to control the PVR, which may be useful for high-frequency applications [59], especially if designed on graphene that is intrinsically a good material for high-frequency operation.

The device investigated here is schematized in figure 11. We consider a TFET designed on a monolayer graphene sheet with finite bandgap $E_G = 200$ meV. The operation and performance of this device has been recently described in detail [49]. Here, we summarize the main results in terms of electrical characteristics. The I–V characteristics obtained for a gate length $L_G = 20$ nm are plotted in figure 12 which shows clearly the modulation of the NDR behaviour, with a PVR reaching here the maximum value of 7.7. However, it should be noted that the PVR is smaller for a higher bandgap of 300 meV with the same doping levels (not shown). Indeed, it is difficult to switch off efficiently the valley current due to the remaining contributions of the thermionic current and interband tunnelling. Actually, as discussed in [9] for graphene

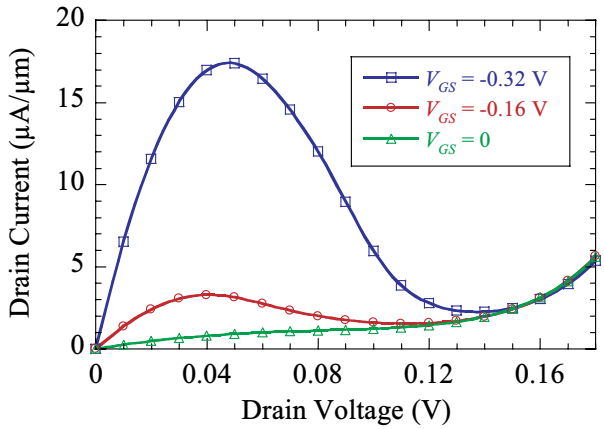

Figure 12. I_D–V_{DS} characteristics of the TFET for the bandgap $E_G = 200$ meV, the gate length $L_G = 20$ nm and the BN gate insulator thickness of 4 nm.

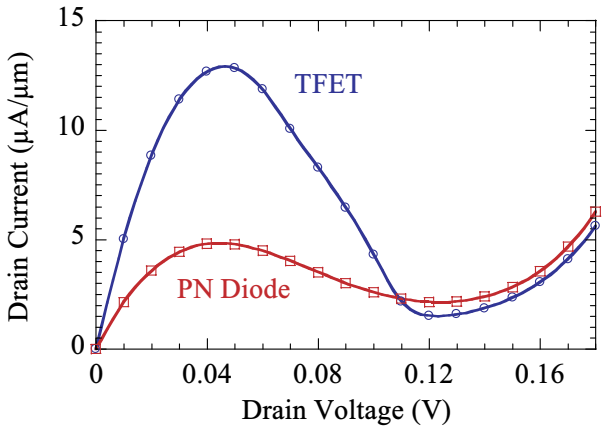

Figure 13. I_D–V_{DS} characteristics of the TFET at $V_{GS} = -0.28$ V for the bandgap $E_G = 200$ meV and the gate length $L_G = 30$ nm, compared to the I–V characteristics of the 2D PN diode of transition length $L = 30$ nm and for the same bandgap.

tunnel diodes the highest PVR is obtained for PN junctions with a potential-energy difference between unbiased source and drain contacts about two times larger than E_G.

With a uniform bandgap in the structure, it is not possible to achieve a PVR as high as in the best tunnel diodes studied above that benefit from an optimization of the position-dependent band structure (sections 3.2 and 3.3). However, this TFET is much less sensitive to the transition (gate) length than the PN diode designed on 2D graphene and compares very well in terms of PVR. Indeed, in figure 13 we compare the I–V_{DS} characteristics of the TFET with $E_G = 200$ meV and $L_G = 30$ nm for $V_{GS} = -0.28$ V with the I–V characteristics of the 'equivalent' PN diode of the same transition length $L = 30$ nm. A much higher peak current is reached in the TFET while the valley current is even smaller than in the PN diode. It makes the TFET a versatile device with tunable non-linear characteristics that can make this device a good option to achieve circuits operating at very high frequency.

3.5. GFET—the effect of chiral tunnelling

An NDR effect has been evidenced experimentally in [28] in the case of long-channel FETs under diffusive transport. It has

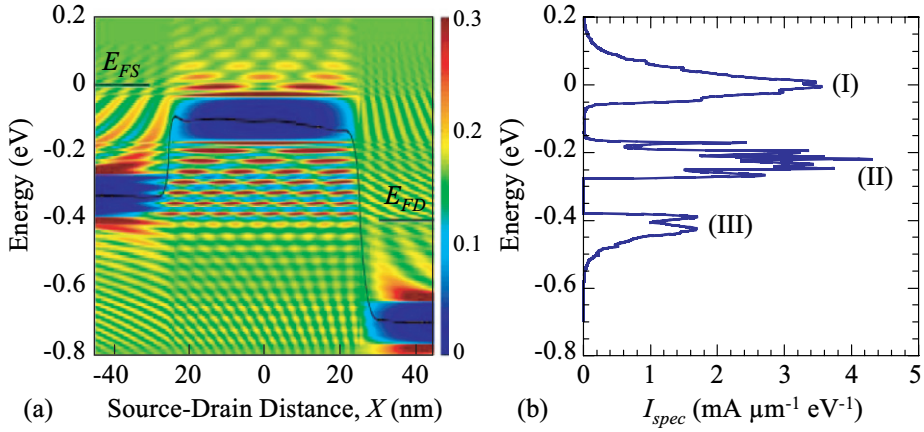

Figure 14. (a) Potential profile at the neutrality point E_K and LDOS in a GFET of gate length $L_G = 50$ nm gate insulator thickness of 2 nm, for the transverse momentum $k_y = K_y + 6.4 \times 10^7$ m^{-1} and the uniform bandgap $E_G = 100$ meV. The gate and drain bias voltages are $V_{GS} = -0.5$ V and $V_{DS} = 0.4$ V, respectively. (b) Corresponding energy spectrum of current at room temperature, with three peaks corresponding to (I) thermionic transmission, (II) chiral tunnelling and (III) band-to-band tunnelling.

been explained as a consequence of the distribution of high local resistance between the N-doped and the P-doped regions of the channel. We show here that in the case of ballistic transport in short-channel, the NDC effect may occur and is explained differently. The schematic structure of simulated devices is the same as that of the TFET in figure 11 but with N-type doping on both sides.

We start with the analysis of the different transport regimes, which is the basis to understand the specific behaviours of graphene transistors. In figure 14(a) we plot the self-consistent results of the LDOS and the potential profile at the charge neutrality point (black solid line) obtained for the gate length $L_G = 50$ nm at gate and drain voltages $V_{GS} = -0.5$ V and $V_{DS} = 0.4$ V, respectively, in the case of a bandgap $E_G = 100$ meV. The LDOS is plotted for a transversal momentum slightly shifted from the charge neutrality point, i.e. for $k_y = (2/3 + 0.005)\pi/a_c\sqrt{3}$ where $a_c = 0.142$ nm is the lattice constant. In figure 14(b) we plot the corresponding energy spectrum of current. For this specific bias point, one can clearly distinguish three peaks in the spectrum, each of them associated with a particular transport regime. At high energy above the gate-induced potential barrier, the peak (I) corresponds to the thermionic transmission regime. The second peak (II) through the barrier corresponds to the chiral tunnelling resulting from the good matching of the hole states in the gated region with the electron states in the source [8]. The third peak (III) is due to the chiral BTB tunnelling between hole states in the source and electron states in the drain. Regimes (I) and (II) are separated by the bandgap in the gated region while regimes (II) and (III) are separated by the bandgap in the source. The separation between these contributions (transmission valleys) is much less pronounced in gapless transistors [60] where it is due only to the k_y-dependent pseudo-energy gap $\hat{E}_G(k_y) = 2t|1 - 2\cos(a_c k_y\sqrt{3}/2)|$ [45]. This pseudo-energy gap is truly zero only for $k_y = K_y = 2\pi/3a_c\sqrt{3}$ (transversal momentum at Dirac point) and finite for $k_y \neq K_y$. For instance, $\hat{E}_G(k_y) \approx 77$ meV for $k_y = K_y + 6.4 \times 10^7$ m^{-1}. Hence, it does not strongly affect the overall transmission of the structure.

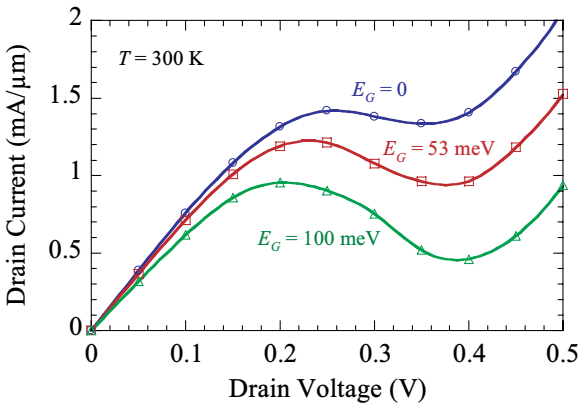

Figure 15. I_D–V_{DS} characteristics of a GFETs of gate length $L_G = 50$ nm for different bandgap values, i.e. $E_G = 0$ meV, $E_G = 53$ meV and $E_G = 100$ meV. The temperature is $T = 300$ K.

In gapless or small-bandgap transistors, the largest contributions to the current usually come from either the chiral tunnelling (at negative V_{GS}) or from the thermionic transmission (at positive V_{GS}). The contribution of the BTB tunnelling is important only in some cases when V_{DS} increases. The Dirac point of the I_D–V_{GS} characteristics, i.e. the off-current, corresponds to the equilibrium of charges in the channel. Hence, it corresponds here to the equilibrium between the chiral tunnelling and thermionic contributions to the current. The former contribution being high in gapless transistors, it follows that the off-current is high and the on/off ratio small.

An NDR effect may actually occur when the transport regime is governed by the chiral tunnelling, i.e. at negative gate voltage ($V_{GS} = -0.5$ V), as shown in figure 15 for different bandgaps. The NDR is small but visible for $E_G = 0$ and increases for finite values of bandgap. The PVR reaches 2.15 for $E_G = 100$ meV at room temperature. To understand this behaviour one should have in mind that the chiral tunnelling is maximum when the transmission window of current transmission (E_{FD}, E_{FS}) is within the gate-induced source–channel barrier, i.e. when the Dirac point in the channel

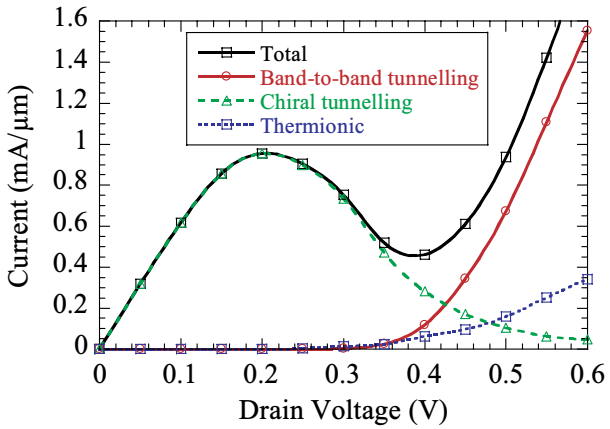

Figure 16. The three contributions to the drain current and the total drain current as a function of drain voltage for a given gate bias $V_{GS} = -0.5$ V. The gate length, bandgap and temperature are 50 nm, 100 meV and 300 K, respectively.

E_{Kch} is higher than E_{FS} and the Dirac point in the source E_{KS} is lower than E_{FD}. It is important to remark that in this regime of transport, the source–channel barrier is very sensitive to V_{DS}: for the gate length $L_G = 50$ nm, the top of the barrier reduces with a rate of about 0.51 eV V^{-1} when V_{DS} is increased in the range (0–0.6 V). Hence, E_{Kch} may go below E_{FS} and/or E_{FD} may go below E_{KS} which both reduce the contribution of chiral tunnelling. Due to the transmission valley between thermionic and chiral tunnelling regimes (pseudo- or real bandgap), there is a V_{DS} range in which the chiral tunnelling decreases and the thermionic current is still limited, as shown in figure 16. At the same time the BTB tunnelling is still limited too (figure 16) because of the transmission valley around the Dirac point in the source E_{KS}. It is the origin of the onset of this NDR mechanism which cannot be observed if the transport is not dominated by the chiral tunnelling through the barrier. The best condition to observe this effect corresponds to the case where the chiral tunnelling tends to reduce, while the increase of both thermionic and BTB (or interband) currents are still limited. This condition is met particularly if, when increasing V_{DS}, E_{Kch} approaches E_{FS} at the same time as E_{FD} approaches E_{KS}.

Since this NDR effect is obviously strongly dependent on the bandgap which generates the transmission valley in the current spectra, it could certainly be optimized using appropriate bandgap nanoengineering, e.g. by inserting GNM sections in the device, as suggested by the results obtained in section 3.3 for tunnel diodes. It is still to be investigated.

4. Conclusion

This work has shown that several physical mechanisms can generate an NDR effect in the I–V characteristics of graphene devices. Quite surprisingly, the simple effect of mismatch of modes between left and right sides of a P^+/P ZGNR junction is shown to induce a significant NDR. However, it is rather sensitive to atomic edge disorder, one of the main limiting factors for practical use of GNR devices. In this respect, it is remarkable that this sensitivity can be strongly reduced in P/N AGNR junctions (tunnel diodes) with appropriate bandgap nanoengineering: by inserting a small or even zero bandgap section in between the P-doped and the N-doped sides of the junction, it is possible to enhance strongly the interband tunnelling in the peak current regime, while the valley current is efficiently limited by the finite bandgap in the doped regions. It gives rise to giant PVR higher than 10^3 at room temperature and, additionally, is weakly dependent on the length of the small-bandgap transition region. Similar results are obtained with GNM tunnel diodes with the possibility of high current level, not limited by the small width of GNRs.

By the action of gate electrode, the tunnel FET offers the additional advantage of tunable peak current and PVR if the bandgap is finite. In comparison with the 2D tunnel diode where the PVR is strongly dependent on the transition length, the gate control of the potential profile in the channel makes the PVR in the TFET higher and weakly sensitive to the gate length. An NDR is shown to possibly occur in a 'conventional' GFET working in chiral tunnelling, i.e. at negative gate voltage. It reaches the value of 2.15 at room temperature for a finite bandgap $E_G = 100$ meV, which may be enough to provide additional functionalities to GFETs.

Regarding the bandgap engineering, though not thoroughly explored in this work, the GNM lattice approach and the possibility to generate position-dependent bandgaps in a graphene sheet certainly open the route to the design of high-performance graphene devices, including transistors.

Acknowledgments

This work was partially supported by the French ANR through projects NANOSIM_GRAPHENE (ANR-09-NANO-016) and MIGRAQUEL (ANR-10-BLAN-0304). One of the authors (VHN) acknowledges the Vietnam National Foundation for Science and Technology (NAFOSTED) for financial support under project no 103.02–2012.42. Another one (VND) acknowledges the Vietnam Ministry of Education and Training (MOET) for support through the project no B2012-01-29.

References

[1] Bolotin K I, Sikes K J, Jiang J, Klima M, Fudenberg G, Hone J, Kim P and Stormer H L 2008 *Solid State Commun.* **146** 351
[2] Zomer P J, Dash S P, Tombros N and van Wees B J 2011 *Appl. Phys. Lett.* **99** 232104
[3] Novoselov K S, Geim A K, Morozov S V, Jiang D, Zhang Y, Dubonos S V, Grigorieva I V and Firsov A A 2004 *Science* **306** 666
[4] Schwierz F 2010 *Nature Nanotechnol.* **5** 487
[5] Cheng R, Bai J, Liao L, Zhou H, Chen Y, Liu L, Lin Y C, Jiang S, Huang Y and Duan X 2012 *Proc. Natl Acad. Sci. USA* **109** 11588
[6] Mizuta H and Tanoue T 1995 *The Physics and Application of Resonant Tunnelling Diodes* (Cambridge: Cambridge University Press)
[7] Dragoman D and Dragoman M 2007 *Appl. Phys. Lett.* **90** 143111
[8] Do V N, Nguyen V H, Dollfus P and Bournel A 2008 *J. Appl. Phys.* **104** 063708
[9] Nguyen V H, Bournel A and Dollfus P 2011 *J. Appl. Phys.* **109** 093706
[10] Fiori G 2011 *IEEE Electron Device Lett.* **32** 1334–6

[11] Nguyen V H, Bournel A, Nguyen V L and Dollfus P 2009 *Appl. Phys. Lett.* **95** 232115
[12] Masum Habib K M, Zahid F and Lake R K 2011 *Appl. Phys. Lett.* **98** 192112
[13] Nguyen V H, Bournel A and Dollfus P 2011 *Semicond. Sci. Technol.* **26** 125012
[14] Song Y, Wu H C and Guo Y 2013 *Appl. Phys. Lett.* **102** 093118
[15] Nguyen V H, Mazzamuto F, Bournel A and Dollfus P 2012 *J. Phys. D: Appl. Phys.* **45** 325104
[16] Ferreira G J, Leuenberger M N, Loss D and Carlos Egues J 2011 *Phys. Rev.* B **84** 125453
[17] Yang H X, Hallal A, Terrade D, Waintal X, Roche S and Chshiev M 2013 *Phys. Rev. Lett.* **110** 046603
[18] Nguyen V H, Bournel A and Dollfus P 2011 *J. Appl. Phys.* **109** 073717
[19] Cresti A, Grosso G and Parravicini G P 2008 *Phys. Rev.* B **77** 233402
[20] Wang Z F, Li Q, Shi Q W, Wang X, Yang J, Hou J G and Chen J 2008 *Appl. Phys. Lett.* **92** 133114
[21] Do V N and Dollfus P 2010 *J. Appl. Phys.* **107** 063705
[22] Cheraghchi H and Esmailzade H 2010 *Nanotechnology* **21** 205306
[23] Ren H, Li Q X, Luo Y and Yang J 2009 *Appl. Phys. Lett.* **94** 173110
[24] Teong H, Lam K T, Khalid S B and Liang G 2009 *J. Appl. Phys.* **105** 084317
[25] González J W, Pacheco M, Rosales L and Orellana P A 2011 *Phys. Rev.* B **83** 155450
[26] Mazzamuto F, Nguyen V H, Apertet Y, Caër C, Chassat C, Saint-Martin J and Dollfus P 2011 *Phys. Rev.* B **83** 235426
[27] Rodríguez-Vargas I, Madrigal-Melchor J and Oubram O 2012 *J. Appl. Phys.* **112** 073711
[28] Wu Y, Farmer D B, Zhu W, Han S J, Dimitrakopoulos C D, Bol A A, Avouris P and Lin Y M 2012 *ACS Nano* **6** 2610–16
[29] Majumdar K, Kallatt S and Bhat N 2012 *Appl. Phys. Lett.* **101** 123505
[30] Giovannetti G, Khomyakov P A, Brocks G, Kelly P J and van den Brink J 2007 *Phys. Rev.* B **76** 073103
[31] Kharche N and Nayak S K 2011 *Nano Lett.* **11** 5274–8
[32] Xu Y, Guo Z, Chen H, Yuan Y, Lou J, Lin X, Gao H, Chen H and Yu B 2011 *Appl. Phys. Lett.* **99** 133109
[33] Fan Y, Zhao M, Wang Z, Zhang X and Zhang H 2011 *Appl. Phys. Lett.* **98** 083103
[34] Xia F, Farmer D B, Lin Y M and Avouris P 2010 *Nano Lett.* **10** 715
[35] Zhang Y, Tang T T, Girit C, Hao Z, Martin M C, Zettl A, Crommie M F, Ron Shen Y and Wang F 2009 *Nature* **459** 820
[36] Bai J, Zhong X, Jiang S, Huang Y and Duan X 2010 *Nature Nanotechnol.* **5** 190–4
[37] Liang X, Jung Y S, Wu S, Ismach A, Olynick D L, Cabrini S and Bokor J 2010 *Nano Lett.* **10** 2454
[38] Oswald W and Wu Z 2012 *Phys. Rev.* B **85** 115431
[39] Nguyen V H, Nguyen M C, Nguyen H V and Dollfus P 2013 *J. Appl. Phys.* **113** 013702
[40] Pedersen J P, Gunst T, Markussen T and Pedersen T G 2012 *Phys. Rev.* B **86** 245410
[41] Yang H X, Chshiev M, Boukhvalov D W, Waintal X and Roche S 2011 *Phys. Rev.* B **84** 214404
[42] Nguyen V H, Do V N, Bournel A, Nguyen V L and Dollfus P 2009 *J. Appl. Phys.* **106** 053710
[43] Reich S, Maultzsch J and Thomsen C 2002 *Phys. Rev.* B **66** 035412
[44] Son Y W, Cohen M L and Louie S G 2006 *Phys. Rev. Lett.* **97** 216803
[45] Castro Neto A H, Guinea F, Peres N M R, Novoselov K S and Geim A K 2009 *Rev. Mod. Phys.* **81** 109–62
[46] Katsnelson M I, Novoselov K S and Geim A K 2006 *Nature Phys.* **2** 620
[47] Fiori G and Iannaccone G 2009 *IEEE Electron Device Lett.* **30** 261–4
[48] Lopez Sancho M P, Lopez Sancho J M and Rubio J 1984 *J. Phys. F: Met. Phys.* **14** 1205–15
[49] Nguyen V H, Niquet Y M and Dollfus P 2012 *Semicond. Sci. Technol.* **27** 105018
[50] Farajian A A, Esfarjian K and Kawazoe Y 1999 *Phys. Rev. Lett.* **82** 5084
[51] Williams J R, DiCarlo L and Marcus C M 2007 *Science* **317** 638
[52] Nakabayashi J, Yamamoto D and Kurihara S 2009 *Phys. Rev. Lett.* **102** 066803
[53] Querlioz D, Apertet Y, Valentin A, Huet K, Bournel A, Galdin-Retailleau S and Dollfus P 2008 *Appl. Phys. Lett.* **92** 042108
[54] Gunlycke D, Areshkin D A and White C T 2007 *Appl. Phys. Lett.* **90** 142104
[55] Nguyen V H, Mazzamuto F, Saint-Martin J, Bournel A and Dollfus P 2011 *Appl. Phys. Lett.* **99** 042105
[56] Nguyen V H, Mazzamuto F, Saint-Martin J, Bournel A and Dollfus P 2012 *Nanotechnology* **23** 065201
[57] Seabaugh A C and Zhang Q 2010 *Proc. IEEE* **98** 2095–110
[58] Leburton J P, Kolodzey J and Briggs S 1988 *Appl. Phys. Lett.* **52** 1608–10
[59] Koga J and Toriumi A 1999 *IEEE Electron Device Lett.* **20** 529–31
[60] Alarcón A, Nguyen V H, Berrada S, Querlioz D, Saint-Martin J, Bournel A and Dollfus P 2013 *IEEE Trans. Electron Devices* **60** 985–91